

Tumbling of asymmetric microrods in a microchannel flow

J. Einarsson,^{1, a)} B. M. Mihiretie,^{1, a)} A. Laas,¹ S. Ankardal,¹ J. R. Angilella,² D. Hanstorp,¹ and B. Mehlig¹

¹⁾*Department of Physics, University of Gothenburg, 41296 Gothenburg, Sweden.*

²⁾*LUSAC, Université de Caen, Cherbourg, France.*

(Dated: 11 November 2021)

We describe results of measurements of the orientational motion of glass microrods in a microchannel flow, following the orientational motion of particles with different shapes. We determine how the orientational dynamics depends on the shape of the particle and on its initial orientation. We find that the dynamics depends so sensitively on the degree to which axisymmetry is broken that it is difficult to find particles that are sufficiently axisymmetric so that they exhibit periodic tumbling ('Jeffery orbits'). The results of our measurements confirm earlier theoretical analysis predicting sensitive dependence on particle shape and its initial orientation. Our results illustrate the different types of orientational dynamics for asymmetric particles predicted by theory.

I. INTRODUCTION

We study experimentally the orientational dynamics of neutrally buoyant non-axisymmetric particles suspended in a viscous shear flow. The rotation of axisymmetric particles in a shear flow has been studied in several experiments (we give a brief account below). The case of non-axisymmetric particles, by contrast, has received little attention experimentally. This is surprising because it is known in theory^{1,2} that the orientational dynamics can be very sensitive to small deviations from the axisymmetric limit. How sensitively the dynamics is affected by slight breaking of axisymmetry depends upon the orientational trajectory which in turn is determined by the initial orientation.

In order to verify this theoretical prediction experimentally it is necessary to use particles with well-defined shapes, to make sure that inertial effects and thermal noise are negligible, and to compare different orientational trajectories of the same particle.

In this paper we describe experimental observations of the orientational motion of micron-sized glass particles suspended in a pressure-driven micro-channel flow. The particles have different shapes: axisymmetric, slightly non-axisymmetric, and substantially non-axisymmetric (the latter are strongly triaxial particles made for the purpose of this experiment by joining two micron-sized glass rods). We verify that inertial and thermal torques have negligible effects by showing that the orientational dynamics is invariant under reversal of the pressure. An optical trap allows us to manipulate the same particle into different initial orientations, to study different orientational trajectories of the same particle. The results of our measurements confirm the predictions of Refs. 1,2, show the sensitive dependence of the orientational dynamics upon particle shape and initial orientation, and qualitatively illustrate the different types of orientational dynamics computed in Refs. 1,2. We have not attempted to quantitatively compare individual experimental particle trajectories with theory, to compare individual trajectories requires to compute the resistance tensors for the actual shape of the particles used in the experiments (the theory of Refs. 1,2 is formulated for ellipsoidal particles). This is beyond the scope of the present paper. Besides the resulting trajectories are of little general interest, they depend very sensitively on the particular shape of the particle in question.

The remainder of this Introduction briefly introduces the relevant theory as well as the wider context of this work. The orientational dynamics of a particle suspended in a viscous flow is determined by resistance tensors that relate the local flow velocity and its gradients to the torque acting on the particle^{3,4}. A given particle shape corresponds to a set of resistance tensors. Their elements are computed by solving Stokes' equations in appropriate geometries^{3,4}. The case of an ellipsoid in a viscous shear flow was first solved by Jeffery⁵. In this limit the equation of motion is given by the condition that the hydrodynamic torque vanishes at every instant. For particles that possess three orthogonal mirror planes⁶, particle shape enters the orientational equation of motion through two parameters, Λ and K . For an ellipsoid with half-axes a , b and c , for example, $\Lambda = (\lambda^2 - 1)/(\lambda^2 + 1)$ and $K = (\kappa^2 - 1)/(\kappa^2 + 1)$ with aspect ratios $\lambda = a/c$ and $\kappa = b/c$.

^{a)}These authors contributed equally to this work.

The case $K = 0$ corresponds to an axisymmetric particle. For axisymmetric particles the orientational dynamics is exactly solvable⁵. When $|\Lambda| < 1$ (so that $0 < \lambda < \infty$) there are infinitely many degenerate periodic orbits, the so-called ‘Jeffery orbits’. This is a consequence of the fact that the dynamical system has a conserved quantity: the ‘orbit constant’. The value of the orbit constant is determined by the initial orientation of the particle. The orientational motion of an axisymmetric particle in a simple shear is sometimes referred to as ‘tumbling’, the particle spends a long time aligned with the flow direction, and it periodically changes orientation by 180 degrees. Different Jeffery orbits differ in the functional form of these periodic ‘flips’. The degeneracy for $K = 0$ is particular to the simple shear flow, and it means that small perturbations can have a large effect.

Inertial forces, for example, are neglected in Jeffery’s theory. These forces induce ‘orbit drift’ into a final stable orbit. This was already suggested by Jeffery⁵, and was discussed in many experimental papers starting with Taylor⁷. See also Ref. 8. The corresponding theory is discussed by Subramanian and Koch⁹ and by Einarsson *et al.*^{10–12}.

Small particles may be affected by thermal noise so that the orbit constant performs a random walk giving rise to a statistical distribution of orientations. This mechanism forms the theoretical basis for understanding the rheology of dilute suspensions^{13,14}.

A third possibility, the topic of this work, is that the particle is not perfectly axisymmetric. This leads to a more complicated orientational equation of motion, also derived by Jeffery⁵. Some numerical examples of its solutions were reported by Gierszewski and Chaffey¹⁵ who found that the motion of a non-axisymmetric particle in a simple shear flow is qualitatively different from that of an axisymmetric particle. Hinch and Leal¹ analysed the structure of the solutions to the equation of motion. They found that for short times a nearly axisymmetric ellipsoidal particle approximately follows a Jeffery orbit, but on longer time scales the ‘orbit constant’ does not remain constant. It oscillates, giving rise to ‘doubly periodic’ tumbling: time series of the components of the unit vector aligned with the major axis of the particle show two distinct periods. Subsequently Yarin *et al.*² inferred from numerical experiments and analytical calculations that ellipsoidal particles may tumble periodically, quasi-periodically, or in a chaotic fashion – depending on the particle shape and on its initial orientation. The term ‘quasi-periodic’ refers to doubly periodic motion with incommensurable periods. Our experimental results support these theoretical predictions: our analysis demonstrates that the tumbling may indeed be periodic, doubly periodic, or possibly chaotic, depending on particle shape and initial orientation. Our results are in good qualitative agreement with theoretical predictions.

This work considers the orientational motion of small neutrally buoyant particles in a time-independent viscous shear flow. This is a special but important case. It is of theoretical interest because of its degeneracy and sensitivity to small perturbations, and it is of practical interest because it fundamentally relates to theories and experiments concerning the rheology of dilute suspensions. Theories are commonly formulated in terms of Jeffery’s equation^{13,16}. Recently there has been a surge of interest in describing the tumbling of non-spherical particles in turbulent^{17–22} and other complex flows^{23–25}. Since it is difficult to solve the coupled particle-flow problem most theoretical and numerical studies rely on Jeffery’s equation as an approximation to the orientational dynamics. Some exceptions are described in Refs. 26–28.

This article is organised as follows. In Section II we enumerate previous experimental efforts to validate Jeffery’s equations. In Section III we describe the experimental setup. Section IV contains our experimental results. These results are discussed in Section V, and we conclude in Section VI.

II. PREVIOUS EXPERIMENTAL WORK

In this section we give a brief account of earlier experiments observing the orientational dynamics of single particles in shear flows.

Taylor⁷ immersed millimeter-sized aluminum spheroids in sodium silicate between two concentric rotating cylinders approximately 10 mm apart. In his brief report he asserts that the tumbling of the spheroids is in qualitative agreement with Jeffery’s predictions, but that the orientational dynamics drifts after many (order of 100) particle rotations.

In a related study Eirich *et al.*²⁹ observed the orientations of glass rods and silk fibres in a Taylor-Couette device. The particles had diameters between 10 and 50 μm and aspect ratios between 5 and 100. No quantitative data on the orientational dynamics was measured, but they observed that the particles tend to align with the flow direction or with the vorticity direction.

Binder³⁰ studied fibers of many different aspect ratios suspended in glycerine. He employed a similar

device with two concentric cylinders and found, as Taylor, that the orientational dynamics slowly drifts.

Mason and co-workers have studied the orientational dynamics of small particles in shear flows during two decades^{31–36}. Initially Trevelyan and Mason³¹ used a setup of two concentric cylinders rotating in opposite directions, making it possible to study a single particle over an extended period of time. The gap between the cylinders was approximately 10 mm, the suspending liquid was white corn syrup, and the particles were 9.5 μm diameter glass fibers cut to different lengths. By observing the particle orientation in a plane orthogonal to vorticity, Trevelyan and Mason³¹ found fairly good quantitative agreement of their experimental results with Jeffery’s theory for one particle rotation (Fig. 7 in Ref. 31). However, for longer time series (up to 30 revolutions) their results were inconclusive: sometimes orbit drift was observed, sometimes not, and sometimes the change of orbit appeared seemingly erratic. In order to compare quantitatively with Jeffery’s equations, valid for spheroidal particles, Trevelyan and Mason fitted the value of Λ to measurements of the tumbling period, yielding in their words an ‘effective aspect ratio’ for cylinders. Bretherton⁶ later showed that this procedure is consistent. Mason and Manley³² extended the experiment to hundreds of particle rotations (Fig. 2 in Ref. 32), but the observed orbit drift was apparently erratic. Mason and Manley mention convective currents as a possible cause for the observed drift, but no conclusions could be drawn concerning the single-particle dynamics. Bartok and Mason³³ used a similar device consisting of concentric cylinders, with a camera-equipped microscope observing along the vorticity axis, allowing to very precisely measure the tumbling behavior of high aspect ratio ($\lambda \approx 45$) acrylic (‘Orlon’) fibres. The experimental results were found to agree quantitatively with Jeffery’s predictions for one particle rotation (Fig. 5 in Ref. 33). However, no data on the orbit drift, if any, was presented. Goldsmith and Mason³⁴ performed the first quantitative measurements of the rotations of disks. They used the same coaxial-cylinder setup described above, with silicone oil for the suspending liquid. The disks were fabricated by heating and compressing polystyrene spheres. The disk diameters were 400–850 μm , and their aspect ratios ranged from $\lambda = 1/20$ to $\lambda = 1/4$. Goldsmith and Mason showed that Jeffery’s theory quantitatively predicts the orientational motion of axisymmetric disks, and that the orbit remained constant over 120 particle rotations (Table II in Ref. 34). In a sequel Goldsmith and Mason³⁵ described measurements of the motion of particles suspended in a liquid flowing through a circular tube. The tube diameters were 2–8 mm, the flow was pressure-driven by a syringe pump, and observations were recorded through a microscope traveling along the tube. Measurements were made on an assortment of particles of sizes ≈ 0.1 mm with aspect ratios ranging from $\lambda = 1/20$ (disks) to $\lambda = 100$ (fibres). Goldsmith and Mason concluded that the dynamics along Jeffery orbits compares well with theory for short times (Fig. 5 in Ref. 35). However, they found measurable orbit drift after a single particle rotation, for both a rod and a disk, see Fig. 7 in the same paper. The drift was attributed to particle asymmetry. Anczurowski and Mason³⁶ fabricated prolate spheroidal particles by polymerising an electrostatically deformed droplet, and showed that Jeffery’s theory holds quantitatively for one particle rotation given the true aspect ratio λ . They used the same concentric-cylinder device described above.

Harris *et al.*³⁷ performed experimental measurements on non-axisymmetric particles ($K \neq 0$). They used an apparatus with counter-rotating cylinders with a gap of 27 mm, which was filled with a glucose solution. The particles were machined from a composite material (‘Tufnol’) into cuboids of 1.75 mm \times 1.28 mm cross-section and 2.5–9.5 mm in length. They measured the unknown elements of the resistance tensors by observing simple rotations around each of the principal axes. With these numerical values of the resistance tensors they compared orientational trajectories of the cuboids to numerical solutions of Jeffery’s equations and found reasonable quantitative agreement for two particle revolutions (Fig. 9 in their paper).

Stover and Cohen³⁸ investigated the effect of a wall on fibre motion using a pressure-driven flow of corn syrup through a rectangular channel. The fibres had cross-sectional diameters of 50 μm and lengths 600 μm , resulting in an aspect ratio of 12. They found that the orientational dynamics are in quantitative agreement with Jeffery’s theory for two particle rotations when the particle is at least one particle length away from the wall.

Kaya and Koser³⁹ observed *E. coli* bacteria advected in a microfluidic channel of rectangular cross section. They found that the orientational motion of the bacteria approximately follows Jeffery orbits.

Einarsson *et al.*²⁷ described examples of orientational trajectories of polymer microrods in a microchannel. They found that the trajectories of some particles were periodic, admitting comparison to Jeffery’s theory. Other trajectories were seen to be aperiodic (Fig. 8 of Ref. 27). The authors suggested that this aperiodic motion may have been caused by lack of axisymmetry of the particle in question. But it was not possible to draw definite conclusions, for several reasons. First the particles were produced by shearing polymer microspheres⁴⁰ which does not produce sufficiently well-controlled shapes. This is a problem because the shape of a given particle in the channel cannot be accurately observed. Second it could not be excluded that thermal torques affected the orientational dynamics. Third, and most importantly, the setup did not

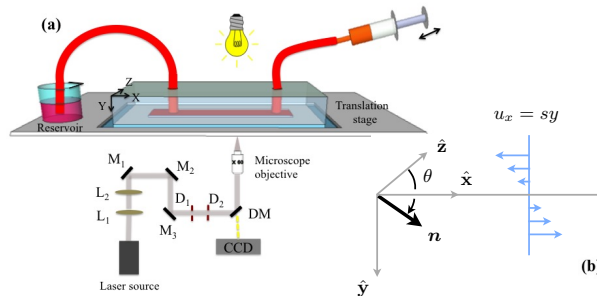


FIG. 1. (a) Schematic picture of the experimental setup, elements are not drawn to scale. $L_{1,2}$: lenses in a Keplerian telescope configuration. $M_{1,2,3}$: mirrors. $D_{1,2}$: diaphragms. DM: dichroic mirror reflecting the laser beam vertically towards the microfluidic system. The microscopic objective focuses the beam on the sample plane. Illumination is provided from the top. (b) Coordinate system in the lab frame spanned by orthogonal unit vectors \hat{x} , \hat{y} , and \hat{z} . The x -axis (flow direction) is directed along the channel length, the y -axis along the depth of the channel, and the z -axis along the channel width. The unit vector \mathbf{n} points along the major axis of the particle. The polar angle between \mathbf{n} and the z -axis is denoted by θ . The particles are kept roughly equally far away from the side walls of the channel. Since the channel is much wider than deep this means that the \hat{y} -direction is the shear direction, so that the local linearisation of the flow-velocity obeys $u_x = sy$ in the frame co-moving with the centre-of-mass of the particle, where s is the shear rate.

allow to record different orientational trajectories of the same particle. This motivated us to perform the experiments summarised in the following, they overcome the problems listed above.

III. METHODS

Fig. 1(a) shows a schematic drawing of the experimental setup to observe the orientational motion of small particles advected in a microchannel flow. A dilute suspension of microrods in a density-matched fluid is introduced into the microchannel. A syringe pump (a standard Harvard Apparatus infuse/withdraw model) is used to drive the flow of the particles. The system is placed under an inverted microscope equipped with a motorised translation stage. A CCD camera is used to register the orientation of a given particle. The initial orientation and position of the particle in the channel is set using an optical trap.

Fig. 1(b) shows the coordinate system that is used in this paper. The x -axis is parallel to the channel length along the flow direction. The y -axis is directed along the depth of the channel. The y -axis is also the optical axis of the microscope objective. The z -axis points along the channel width. The orientation of the particle is determined by the unit vector \mathbf{n} along the major axis of the particle.

The experiment is performed with cylindrical glass rods with diameters $3 \mu\text{m} \pm 0.01 \mu\text{m}$ (PF-30S, Nippon Electric Glass Co., Ltd). The microrods were manufactured as spacers in liquid-crystal devices (PF-30S, Nippon Electric Glass Co., Ltd). This requires precise diameters. The lengths of the rods vary between approximately $10 \mu\text{m}$ and $30 \mu\text{m}$. An electron-microscope image of the particles is shown in Fig. 2(a). This Figure shows that the end surfaces of the cylindrical rods are randomly inclined and uneven, indicating that the particles were obtained by breaking longer glass rods. While this is irrelevant for the intended industrial use as spacers, it is important for our application. Random inclinations of the end surfaces break axisymmetry: sometimes only very slightly [lower left particle in Fig. 2(a)], sometimes more [c.f. particle in the centre of Fig. 2(a)]. We investigate the orientational dynamics of highly asymmetrical particles by studying aggregates of glass rods. Following Lewandowski *et al.*⁴¹ a dilute suspension of microrods is left to evaporate in order to produce double particles, Fig. 2(b)–(d). The glass particles have an index of refraction of 1.56 and a density of $\rho_p = 2.56 \text{ g cm}^{-3}$.

To achieve neutral buoyancy the fluid must have the same density as the particles. To this end we mix 22.2%wt water, 4.4%wt glycerol, and 73.4%wt sodium metatungstate monohydrate (Alfa Aesar GmbH). Density matching is achieved by titration while observing the particle under the microscope until the particle is buoyant for several minutes. But there are additional sources of error that are difficult to control. For example, when the fluid is pumped through the microchannel minute changes in temperature are expected to slightly change the fluid density. Such changes could induce small variations in the y -position of the particle that we sometimes observe during the recordings. The suspension is highly diluted in order to avoid

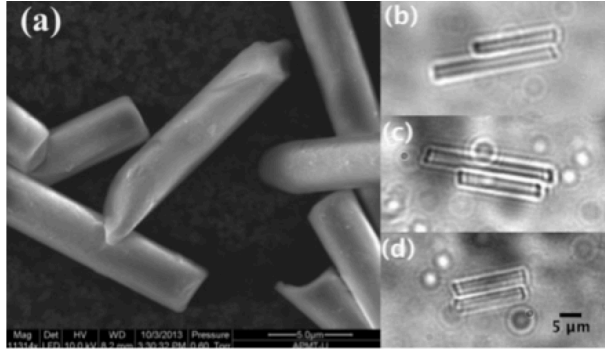


FIG. 2. (a) Electron-microscope image of the glass particles used in the experiments. Taken by S. Gustafsson, Chalmers. (b-d) Optical-microscope images of the double particles used in the experiments. The angular dynamics of the particle in panel (b) is shown in Fig. 5, panel (c) corresponds to Fig. S8, and panel (d) to Fig. S9. The last two figures are found in the Supplementary Online Material⁴².

particle-particle interactions. The mixture has a viscosity of $\mu = 25 \text{ mPa s}$ at 20°C . We estimate the shear Reynolds number $\text{Re}_s = \rho_f s a^2 / \mu$ as follows. The particle length a is of the order of $20 \mu\text{m}$. The shear rate s is determined by the flow speed u_x which is in turn given by the flow rate $8 \mu\text{l}/\text{min}$ and the cross section of the channel, $2.5 \text{ mm} \times 200 \mu\text{m}$. This results in $u \approx 0.3 \text{ mm s}^{-1}$ and a shear rate of $s \approx 3 \text{ s}^{-1}$ at $60 \mu\text{m}$ depth assuming a parabolic profile in the y -direction, and that the channel is much wider than deep. The density of the fluid ρ_f equals the particle density, $\rho_p = 2.56 \text{ g cm}^{-3}$. This gives $\text{Re}_s \approx 10^{-4}$. Inertial effects are thus negligible on the time-scale of the experiment.

The microchannel is produced using standard soft lithography. The process begins by milling a rectangular moulding form in aluminum. The surfaces of the mould are mechanically polished. A 10:1 mixture of polydimethylsiloxane (PDMS) and sylgard 184 Dow Corning (Sigma Aldrich) is poured on the moulding form and allowed to cure for several hours. The PDMS replica obtained after peeling off the mould is sealed to a glass slide (thickness 0.17 mm) by oxygen plasma bonding. This results in a rectangular channel that is 40 mm long, 2.5 mm wide, and $150 \mu\text{m}$ deep. For some measurements, a channel with a depth of $200 \mu\text{m}$ was used, see Table I. The suspension is injected into the channel using thin tubing connected to a syringe pump. PTFE tubes (Cole-Parmer) with outer diameters of 0.76 or 1.07 mm are used, the former in connection with a plastic syringe (1 ml , Terumo), the latter in connection with a glass syringe ($500 \mu\text{l}$, Hamilton).

The optical system is built around a Nikon X60 microscope objective (NA 1.0, WD 2 mm). The particle motion is recorded with a CCD video camera (Leica). The channel is mounted on a translation stage that moves the microchannel over the fixed observation microscopic objective. The stage is driven by a stepper motor that records the position of the stage. By moving the channel a given particle is kept within the field of view of the objective, despite the fact that the particle is advected by the fluid through the microchannel.

A single-beam optical trap is used to set the initial orientation and position of a given particle. The optical trap makes use of the microscope objective (Fig. 1), it provides sufficient magnification to not only visualise the particle, but also to trap it with a continuous infrared laser of wavelength 1075 nm (10 W , IPG-Laser GmbH). The most efficient way of trapping a glass rod with this setup is to direct the laser beam towards one of the two ends of the particle. Different orientations can be imposed on the particle by moving the channel sufficiently quickly to cause one end of the particle to leave the trap, yet sufficiently slowly so that the other end of the particle is kept trapped.

The experimental procedure described above ensures stable and reproducible experimental conditions. But a number of external factors were difficult to control and could still influence the experimental results to a small degree: evaporation due to the presence of unsaturated air in the reservoir, the presence of air bubbles in the channel that are difficult to get rid of, and pressure drops inside the channel due to the elasticity of the PDMS structure.

We use the image-analysis algorithm employed by Einarsson *et al.*²⁷. Images are acquired at a rate of 100 frames per second. Each frame is stored as 8-bit gray-scale bitmap with 692×520 pixels. The pixel size is $0.21 \mu\text{m}$. For a given frame the image analysis proceeds in three basic steps. First static noise is reduced by subtracting the time-averaged intensity from each frame. Then the boundary of the projection of the particle into the image plane is detected, and finally an ellipse is fitted to the boundary. Details are given in Ref. 27. The output defines the position and the orientation of the particle in the image. The centre-of-mass coordinates of the particle in the laboratory frame are determined using the output from the stepper motor

recording the position of the stage.

The main sources of uncertainty in the image analysis are the limited resolution of the camera and diffraction. The latter gives rise to a diffuse particle boundary. The uncertainty in the determination of the particle orientation is largest when the short end of the rod faces the camera, i.e. for small values of n_z (see Fig. 1).

A typical experiment starts by capturing a particle with the optical trap. The particle is brought into the desired location in the x - z -plane by moving the channel. All particles are started close to one of the inlets at approximately equal z -distances to both side walls. We verified that the z -position remains centred, with an error typically at most one particle length. This implies that the shear in the z -direction remains very small (the channel is much wider than deep). The y -coordinate thus corresponds to the shear direction, and the z -coordinate is the vorticity direction. The particle is brought to the desired initial orientation as described above and the centre-of-mass of the particle is placed at a depth of 60 μm . The precision in determining the initial depth is determined by the depth-of-field of the microscope. It is estimated to be of the order of one particle length. Then the particle is released to follow the flow in the microchannel. We then invert the pressure gradient so that the particle is advected back in the opposite x -direction. For each orientational trajectory we record both forward and backward dynamics. Since Stokes' equation is invariant under simultaneous pressure inversion and time reversal, the backward dynamics must exactly retrace the forward dynamics unless irreversible effects such as inertia or thermal noise affect the dynamics. Examples for the resulting video-microscopy recordings of the orientational dynamics in the x - z -plane can be viewed via the MULTIMEDIA VIEW links in Figs. 3 and 5.

For a given particle this procedure is repeated many times to obtain orientational trajectories with different initial orientations. We record the length of the projection of the particle into the x - z -plane as a function of time. We estimate the particle length using the procedure described in Ref. 27. Once the particle length is known we can extract the components of the unit vector \mathbf{n} determining the orientation of the particle, as a function of time.

We plot the orientation not as a function of time but as a function of distance that the centre-of-mass of the particle has traveled through the channel, advected by the flow:

$$x(t) = \int_0^t dt' u_x(t'). \quad (1)$$

Here $u_x(t)$ is the instantaneous flow velocity at time t . This transformation simplifies the analysis because it accounts for the fact that the shear-rate is time-dependent: the flow velocity changes when the pressure is reversed, and in order to avoid inertial effects these reversals must be performed slowly. The invariance of Stokes equation under time and pressure reversal implies $x(t) = -x(-t)$. We overlay forward and backwards dynamics by plotting the orientation as a function of centre-of-mass position.

IV. EXPERIMENTAL RESULTS

Figures 3, 4, and 5 show orientational dynamics of three different particles. For each particle five different orientational trajectories are shown, corresponding to different initial orientations [panels (b) to (f)]. In all three Figures we show trajectories of the x - and z -components of the unit vector \mathbf{n} that points along the major axis of the particle. Here n_x is the component in the flow direction, and n_z is the component in the vorticity direction. The third component of \mathbf{n} is determined by normalisation, $|\mathbf{n}| = 1$.

In panel (a) of each Figure we summarise the orientational dynamics by recording the values of n_z whenever $n_x = 0$. We denote the resulting sequence of consecutive n_z -values by $n_z^{(i)}$, $i = 1, 2, 3, \dots$. For an axisymmetric particle Jeffery's equation predicts that $n_z^{(i+1)} = n_z^{(i)}$, shown as the solid line along the diagonal in panel (a).

As mentioned above, the particle is first advected along a stream line of the pressure-driven flow in the channel. We then invert the pressure gradient so that the centre-of-mass of the particle is advected back to where it came from. For each orientational trajectory we show the 'forward dynamics' (blue solid line), going from right-to-left in the Figure. After the reversal follows the 'backward dynamics' (red dashed line). Since Stokes' equation is invariant under simultaneous pressure inversion and time reversal, the backward orientational dynamics must exactly retrace the forward dynamics unless irreversible effects due to inertia or thermal noise affect the dynamics noticeably on the time-scale of the experiment.

Consider first the trajectories shown in Fig. 3, corresponding to particle 1. Panels (b) to (f) show orientational trajectories of n_x and n_z for different initial orientations. In all cases the backward dynamics retraces

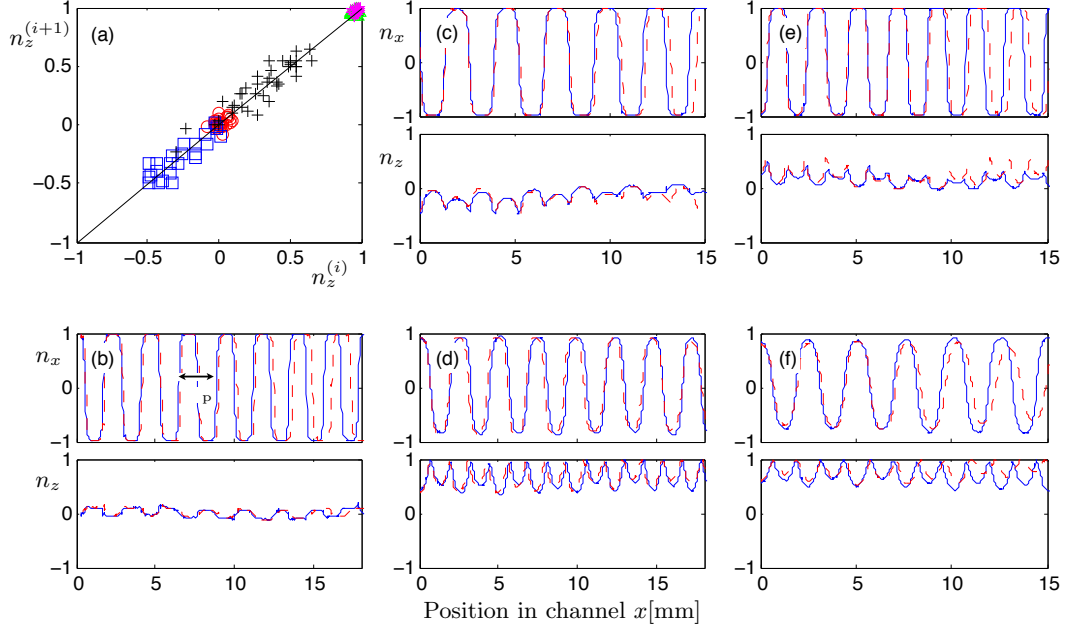


FIG. 3. Orientational dynamics of particle 1. (a) Dynamics of n_z . Here $n_z^{(i)}$ denote the values of n_z at subsequent zero crossings of n_x , $i = 1, 2, 3, \dots$. The data are taken from panels (b-f). Red \circ data from panel (b); blue \square from (c); green \triangle data from (d); black $+$ data from (e); magenta \star data from (f). Panels (b-f) show orientational dynamics as a function of c.o.m.-position x in the channel, Eq. (1). Data in different panels correspond to different initial orientations. Solid blue and dashed red lines represent forward and backward trajectories, respectively. The flow direction is reversed at $x = 0$. The horizontal arrow in panel (b) indicates the period X_p [mm] of the trajectory. The video-microscopy recording of the orientational dynamics shown in panel (b) can be viewed at [MULTIMEDIA VIEW](#), that of panel (d) at [MULTIMEDIA VIEW](#).

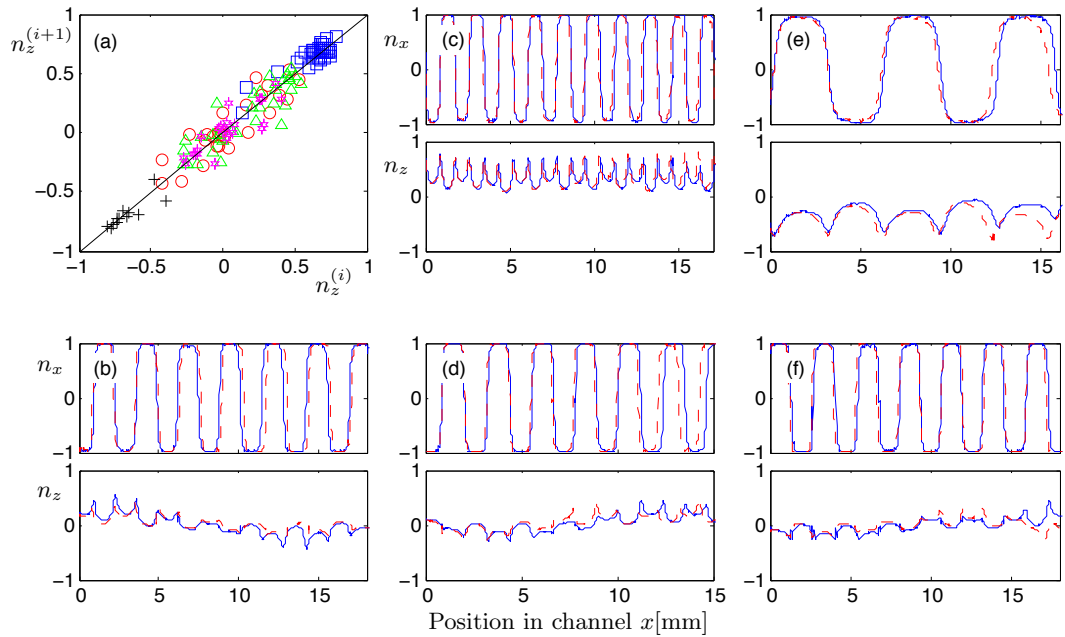


FIG. 4. Orientational dynamics of particle 2. See caption of Fig. 3 for details.

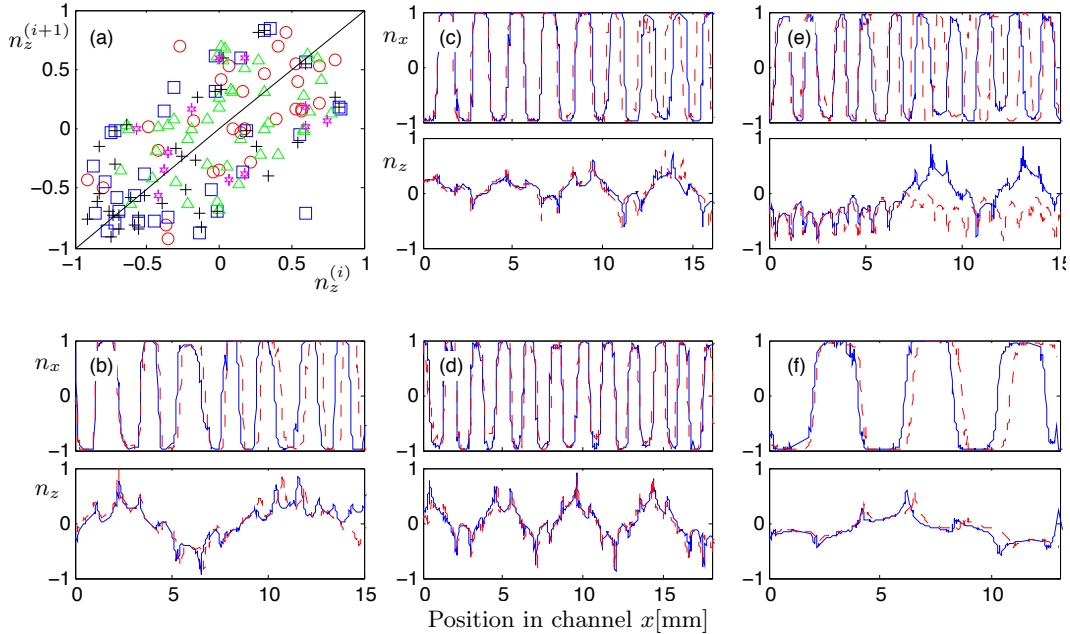


FIG. 5. Orientational dynamics of particle 3. See caption of Fig. 3 for details. The video-microscopy recording of the orientational dynamics shown in panel (d) can be viewed via [MULTIMEDIA VIEW](#)

the forward dynamics very well. This shows that neither inertial forces nor rotational diffusion affect the orientational dynamics. We attribute the small dephasing visible in each panel to a small density mismatch (discussed in Section III), causing the particle to sink (or float), changing the shear rate it experiences. Apart from this slight dephasing all orientational trajectories are fairly periodic. For a given n_x -trajectory the relative variation of the centre-of-mass distance between two consecutive $n_x = 0$ -events (‘half-period’) is of the order of 10%. Between different panels we observe variations in the period X_p , between 2.1 mm and 2.6 mm, caused by the uncertainty in the y -position mentioned above. Panel (a) indicates that $n_z^{(i+1)}$ is approximately equal to $n_z^{(i)}$.

Fig. 4 shows the orientational dynamics of particle 2 for different initial orientations [panels (b) to (f)]. In all cases the backward dynamics retraces the forward dynamics well, at least for a few millimetres. As for particle 1 the trajectories show a slight dephasing within each panel. Different panels show quite different periods X_p , ranging between 1.7 mm and 5.9 mm. In panels (d) and (f) we see that the amplitude of n_z changes aperiodically. This is also apparent from panel (a) exhibiting a somewhat wider scatter around the diagonal than panel (a) in Fig. 3.

Fig. 5 shows the orientational dynamics of particle 3, an asymmetric double particle. For all initial orientations the backward dynamics retraces the forward dynamics fairly well, with the exception of the trajectories shown in panel (e). As for particles 1 and 2 we observe a slight dephasing within each panel. The dynamics of n_x is quite periodic, but again the periods X_p vary from panel to panel, ranging from 1.4 mm to 4 mm. In all cases n_z shows distinct aperiodicity. Panel (a) exhibits a larger scatter around the diagonal than panel (a) in Fig. 4.

The orientational dynamics of particles 1, 2, and 3 was obtained under slightly different experimental conditions. These are summarised in Table I, as well as the particle properties. Table I also gives information about other particles for which we obtained precise orientational dynamics. The corresponding Figures are found in the Supplementary Online Material⁴².

Video-microscopy recordings corresponding to the data shown in Figs. 3(b), (d), and 5(d) can be viewed via the [MULTIMEDIA VIEW](#) links in the corresponding figure captions.

Particle number	Particle type ^a	Particle length(μm) ^b	Channel depth (μm)	Flow rate ($\mu\text{l}/\text{min}$)	Figure
Particle 1	single	20.5	200	8	Fig. 3
Particle 2	single	24.3	150	5	Fig. 4
Particle 3	double ^c	28.7	200	8	Fig. 5
Particle 4	single	20.1	150	7.5	Fig. S1 ^d
Particle 5	single	29.5	200	8	Fig. S2
Particle 6	single	17	150	5	Fig. S3
Particle 7	single	25	150	5	Fig. S4
Particle 8	single	26.5	150	5	Fig. S5
Particle 9	single	22.5	150	7.5	Fig. S6
Particle 10	single	25.5	150	5	Fig. S7
Particle 11	double ^e	26	200	8	Fig. S8
Particle 12	double ^f	17	200	8	Fig. S9

TABLE I. Description of particles and other experimental parameters. ^aSingle or double particle. ^bParticle length as extracted from image-analysis algorithm, see Section III. We estimate the error to be of the order of $1\mu\text{m}$. ^cThis particle is shown in Fig. 2(b). The lengths of the two glass rods are 26.4 and $17.3\mu\text{m}$. ^dThese Figures are in the Supplementary Online Material⁴². ^eThis particle is shown in Fig. 2(c). The lengths of the two glass rods are 26 and $16.5\mu\text{m}$. ^fThis particle is shown in Fig. 2(d). The lengths of the two glass rods are both $16\mu\text{m}$.

V. DISCUSSION

The results summarised in Figs. 3 to 5 show the orientational dynamics of single and double glass rods. In general the particles are not perfectly axisymmetric (as seen in Fig. 2), and therefore do not follow perfect Jeffery orbits. In this section we relate our experimental results to the theoretical predictions valid for ellipsoidal particles^{1,5}. The particles in our experiment do not satisfy the mirror symmetries assumed in this theory, but it is plausible that the effects of breaking axisymmetry predicted by this theory apply at least qualitatively to our glass rods.

The equation of motion for the orientational dynamics of an ellipsoidal particle^{1,5} can be cast in the form⁴³

$$\dot{\mathbf{n}} = \mathbb{O}\mathbf{n} + \Lambda (\mathbb{S}\mathbf{n} - (\mathbf{n} \cdot \mathbb{S}\mathbf{n})\mathbf{n}) + \frac{K(1 - \Lambda^2)}{K\Lambda - 1} (\mathbf{n} \cdot \mathbb{S}\mathbf{p})\mathbf{p}, \quad (2a)$$

$$\dot{\mathbf{p}} = \mathbb{O}\mathbf{p} + K (\mathbb{S}\mathbf{p} - (\mathbf{p} \cdot \mathbb{S}\mathbf{p})\mathbf{p}) + \frac{\Lambda(1 - K^2)}{K\Lambda - 1} (\mathbf{n} \cdot \mathbb{S}\mathbf{p})\mathbf{n}. \quad (2b)$$

Following the convention outlined in Section III, \mathbf{n} is a unit vector that points along the major axis of the ellipsoidal particle. The unit vector \mathbf{p} is orthogonal to \mathbf{n} , directed along the particle axis corresponding to the length b used in the definition of the aspect ratio κ (defined in the Introduction). The geometry of the ellipsoid is characterised by the two shape parameters Λ and K that are defined in the Introduction, Section I. The matrices \mathbb{S} and \mathbb{O} are the symmetric and anti-symmetric parts of \mathbb{A} , the matrix of fluid-velocity gradients. In our case this matrix takes the form

$$\mathbb{A} = \begin{bmatrix} 0 & s & 0 \\ 0 & 0 & 0 \\ 0 & 0 & 0 \end{bmatrix}, \quad (3)$$

where s is the shear strength (Fig. 1).

Eqs. (2) are symmetric under the simultaneous exchange of \mathbf{n} and \mathbf{p} as well as Λ and K : describing the motion of the same particle using a different coordinate system within the particle must result in the same dynamics. Note also that the non-linear coupling between \mathbf{n} and \mathbf{p} involves the strain \mathbb{S} only. This coupling maintains orthogonality of the two vectors \mathbf{n} and \mathbf{p} . The anti-symmetric part \mathbb{O} just causes a solid-body rotation. For axisymmetric particles, $K = 0$, so that the tumbling of \mathbf{n} becomes independent of the dynamics of \mathbf{p} (but not vice versa). The resulting equation for \mathbf{n} has infinitely many degenerate periodic solutions, the Jeffery orbits⁵. The dynamics of \mathbf{p} describes how the particle spins around its symmetry axis.

When $K \neq 0$ (and $\Lambda \neq 0$), no general closed-form solutions of Eqs. (2) are known. It is convenient to represent the numerical solutions of Eq. (2) in terms of a Poincaré surface-of-section⁴⁴, recording the locations

at which the dynamics intersects a surface in the phase space of Eq. (2). This section is constructed as follows. Hinch and Leal¹ have shown that the vector \mathbf{n} rotates around the vorticity at a positive angular velocity so that one can reduce the dimensionality of the problem by parametrising the orientational dynamics in terms of the corresponding angle. A suitable condition^{1,2} defining the surface-of-section is that \mathbf{n} is perpendicular to the flow direction, $n_x = 0$. Following Yarín *et al.*² we take the coordinates in the surface-of-section to be ψ and n_z , where ψ is the Euler angle parametrising the spin of the particle around the axis \mathbf{n} , and n_z is the z -component of \mathbf{n} , the cosine of the angle θ between \mathbf{n} and vorticity (Fig. 1). When $n_x = 0$ we record the coordinates (ψ, n_z) . To define the Euler angles (θ, ϕ, ψ) we use the convention of Goldstein⁴⁵ and express \mathbf{n} and \mathbf{p} as

$$\mathbf{n} = \begin{bmatrix} \sin \theta \sin \phi \\ -\sin \theta \cos \phi \\ \cos \theta \end{bmatrix}, \quad \text{and} \quad \mathbf{p} = \begin{bmatrix} -\sin \psi \cos \phi - \cos \theta \sin \phi \cos \psi \\ -\sin \psi \sin \phi + \cos \theta \cos \phi \cos \psi \\ \cos \psi \sin \theta \end{bmatrix}. \quad (4)$$

So θ is the polar angle depicted in Fig. 1. The angle ϕ is referred to as the ‘precession angle’. This angle measures the direction of the projection of \mathbf{n} into the flow-shear plane. Eqs. (2) correspond to Eqs. (2.1) and (2.2) in Ref. 2, setting $s = -1$ and defining the aspect ratios λ and κ in terms of the particle axes² as follows: $a_x = \lambda a_z$ and $a_y = \kappa a_z$.

In the experimental time series shown in Figs. 3 to 5, instances where $n_x = 0$ correspond to peaks in the oscillation in n_z . The n_z -coordinate in the surface-of-section is therefore easily read off from the experimentally observed time series. The angle ψ , by contrast, cannot be measured in our experiment because we cannot track how the particles spin around \mathbf{n} .

Four different surfaces-of-section are shown in Fig. 6, obtained by numerical integration of Eqs. (2) for a large number of different initial orientations, and plotting the sequence $[\psi^{(i)}, n_z^{(i)}]$ of (ψ, n_z) evaluated at consecutive zero crossings of n_x , labeled by $i = 1, 2, 3, \dots$. Similar sections are found in Ref. 2. The map that gives $[\psi^{(i+1)}, n_z^{(i+1)}]$ in terms of $[\psi^{(i)}, n_z^{(i)}]$ is called the Poincaré map.

Fig. 6(a) depicts the orientational dynamics of an axisymmetric particle, $K = 0$. The coordinate n_z is a conserved quantity on the surface-of-section, Jeffery orbits appear as horizontal lines in Fig. 6(a), one-parameter families parametrised by ψ . In the literature Jeffery orbits are commonly identified by their orbit constant C . It is given by the value of $\tan \theta$ at $n_x = 0$ (see for example Eq. (3) in Ref. 1). In this paper we characterise Jeffery orbits by $n_z = \cos \theta = 1/(1 + C^2)$ on the surface-of-section ($n_x = 0$). Fig. 6(a) illustrates that the orientational dynamics depends on the initial orientation, determining the value of n_z . We remark that the periods of \mathbf{n} and ψ are not in general commensurate for $K = 0$. But the tumbling of \mathbf{n} is independent of that of the angle ψ and thus periodic for axisymmetric particles.

Fig. 6(b) shows the orientational dynamics of a weakly asymmetric ellipsoidal particle ($K \approx 0.095$ and $\Lambda = 12/13$). We see that Jeffery orbits with $n_z \approx \pm 1$ remain almost unchanged. But there are substantial changes for smaller values of $|n_z|$, compared with the surface-of-section for $K = 0$. We see that n_z ceases to be a constant of motion, doubly-periodic orientational dynamics results. The most substantial changes occur near $n_z = 0$. The $n_z = 0$ -Jeffery orbit is replaced by two fixed points at $(0, 0)$ and $(\pm\pi/2, 0)$ on the surface-of-section.

This fact and the surface-of-section patterns in the vicinity of these points follow from the time-reversal symmetry of Eqs. (2). The general principle is explained in Section 6.6 of Ref. 44. See also Ref. 46. The invariance of Stokes equation referred to in Section III implies that Eqs. (2) are invariant under

$$t \rightarrow -t, \quad n_x \rightarrow -n_x, \quad \text{and} \quad p_x \rightarrow -p_x. \quad (5)$$

The fixed point $(0, 0)$ is mapped onto itself under this transformation. It follows that the dynamics in its immediate neighbourhood can neither be expanding nor contracting. In other words the determinant describing the linearised motion in the vicinity of this fixed point,

$$\det \begin{bmatrix} \frac{\partial \psi^{(i+1)}}{\partial \psi^{(i)}} & \frac{\partial \psi^{(i+1)}}{\partial n_z^{(i)}} \\ \frac{\partial n_z^{(i+1)}}{\partial \psi^{(i)}} & \frac{\partial n_z^{(i+1)}}{\partial n_z^{(i)}} \end{bmatrix}, \quad (6)$$

must be of unit modulus despite the fact that the dynamics (2) is dissipative. We find numerically that the eigenvalues are $\exp(\pm i\sigma)$. The point $(0, 0)$ is thus an elliptic fixed point, surrounded by a one-parameter family of closed orbits that appear as concentric closed curves, much like so-called ‘tori’ in so-called ‘Hamiltonian’ systems with area-preserving phase-space dynamics⁴⁷. For near-axisymmetric particles Hinch and

Leal¹ analysed the corresponding orbits by multiple-scales analysis. As these orbits rotate around the elliptic point, the value of n_z changes sign. This doubly-periodic motion may be quasi-periodic or periodic, depending on whether the two frequencies are incommensurate or not (corresponding to irrational or rational winding numbers, respectively).

The point $(\pm\pi/2, 0)$ is a hyperbolic fixed point. We find numerically that the eigenvalues are real and opposite, γ and γ^{-1} . The fact that the $n_z = 0$ -orbit is destroyed upon infinitesimal perturbation and replaced by a discrete set of fixed points of alternating stability is typical for Hamiltonian systems⁴⁷. The mechanism in our dissipative system is analogous, a consequence of the symmetry (5).

For larger asymmetries chaotic orientational dynamics occurs, seen as a region with a stochastic scatter of points in Fig. 6(c). Almost all Jeffery orbits are modified, only those with n_z close to ± 1 remain. Whether the orientational dynamics is periodic, quasi-periodic, or chaotic depends upon the initial condition on the surface-of-section.

Fig. 6(d) shows the orientational dynamics for ellipsoidal particles with $K = 3/5$ and $\Lambda = 12/13$. This value of K is similar the corresponding value for the double particle 3 (Figs. 2(b) and 5), but this particle has $\Lambda \approx 40/41$. We do not seek quantitative correspondence between these parameters because the particles used in our experiment are not ellipsoidal. This prevents us from drawing quantitative conclusions, but still allows for a qualitative comparison between theory and experiment. The orientational dynamics displayed in Fig. 6(d) is either on tori or chaotic. Motion on tori can occur with large amplitudes, so that n_z changes from $n_z \approx -1$ to $n_z \approx 1$.

How are these observations reflected in the experimental time series shown in Figs. 3 to 5? Since we cannot measure the angle ψ in our experiments, we concentrate on the dynamics of n_z . Fig. 7 shows the range of changes of n_z in one iteration of the Poincaré map for particles with different degrees of asymmetry, determined by numerically recording the changes $n_z^{(i+1)} - n_z^{(i)}$ along orientational trajectories. The diagonal corresponds to symmetric particles where $n_z^{(i+1)} = n_z^{(i)}$. The larger the asymmetry, the larger is the range of $n_z^{(i+1)} - n_z^{(i)}$ that may occur, reflecting the properties of the surfaces-of-section shown in Fig. 6.

Fig. 7 can be directly compared with Figs. 3(a) to 5(a). Our experimental results show that the Poincaré map may scatter significantly around the diagonal. The above discussion explains that this is a consequence of doubly-periodic and possibly chaotic orientational dynamics of asymmetric particles. The range of scatter differs between different particles, a consequence of different degrees of asymmetry. We see that the scatter is largest for the double particle 3, with $K \approx 3/5$ [Fig. 5(a)]. Particle 1, by contrast, shows only negligible scatter around the diagonal [Fig. 3(a)]. We infer that this particle is highly symmetric, K is very small. The data shown in Fig. 3 are consistent with the conclusion that particle 1 follows Jeffery orbits, n_z remains approximately constant in the surface-of-section. But we remark that the shape of the $n_z \approx 0$ -orbit does not look like a Jeffery orbit for an axisymmetric particle. We cannot exclude that this is due to possible non-ellipsoidal deviations from axisymmetry. The surface-of-section dynamics is most sensitive to such shape perturbations near $n_z = 0$. A more likely explanation is that the shape of the trajectory is a consequence of systematic (and reproducible) tracking errors due to diffraction and finite pixel size. These errors are largest for small values of n_z , as discussed in Section III.

Particle 2 is also a single glass rod, but it shows a somewhat larger range of scatter around the diagonal [Fig. 4(a)]. We attribute this to a more substantial breaking of axisymmetry at the tips of the particle [as seen for instance in Fig. 2(a)]. Particle 2 shows fairly periodic motion for $n_z \approx 1$ and distinctly doubly-periodic orientational dynamics for small values of n_z . This confirms that the initial orientation determines whether the particle tumbles periodically or aperiodically. Note also that n_z changes sign along the trajectories that remain near $n_z = 0$ [Fig. 4(b), (d), and (f)]. All of these observations are qualitatively consistent with the surfaces-of-section shown in Fig. 6(b) and 6(c).

For particle 3 the value of n_z changes sign for all orientational trajectories shown. This is consistent with the fact that the Fig. 6(d) shows predominantly this type of motion. Fig. 5(e) is consistent with chaotic orientational motion in the stochastic layer around the elliptic island. The surfaces-of-section in Fig. 6 show that there are two types of doubly-periodic motion: either n_z has the same sign, or its sign changes periodically. The trajectory in Fig. 5(e) exhibits both behaviours, indicating chaotic dynamics. Now consider the trajectory shown in Fig. 5(c). It is not periodic or doubly-periodic, but the reversal works well (at least initially). But we cannot conclude that the dynamics is consistent with surfaces-of-section discussed above. The n_z -values at $n_x = 0$ in Fig. 5(c) change from approximately 0.25 to 0.75 in modulus. Explaining this behaviour in terms of chaotic dynamics on the surfaces-of-section requires a large stochastic region, larger than the one shown in Fig. 6(d). This might mean that the trajectory shown in panel (d) is a doubly-periodic piece of a chaotic trajectory that may show different behaviours at larger times. But to determine whether these behaviours can be explained by chaotic dynamics would require to derive and

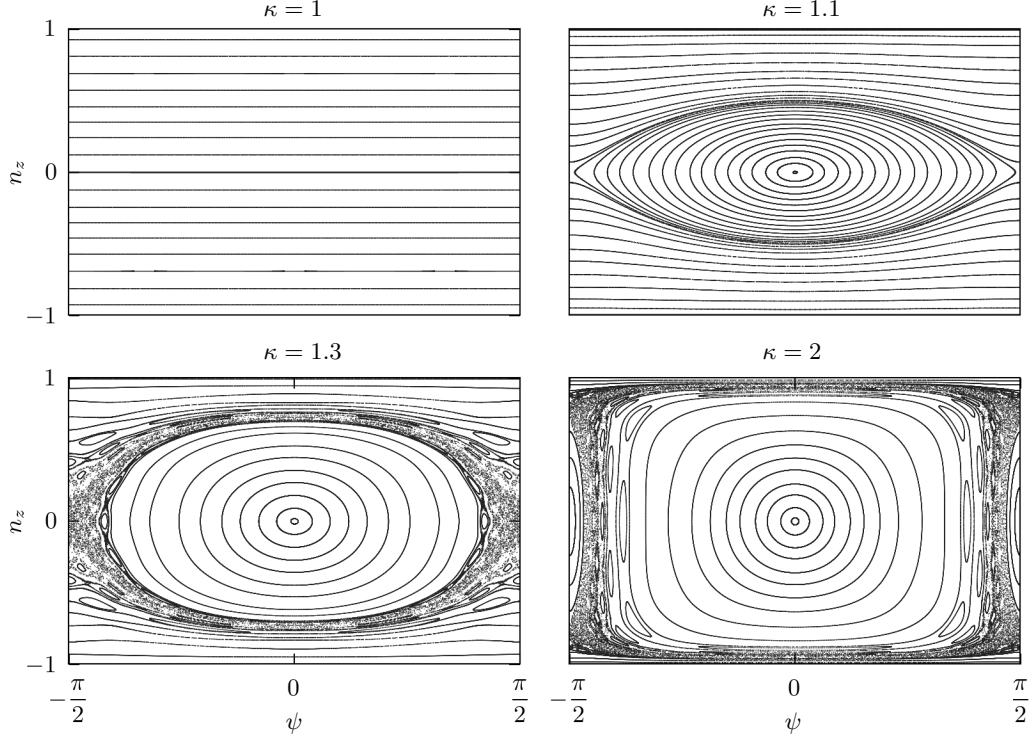


FIG. 6. Poincaré surfaces-of-section for $\Lambda = 12/13$ and different values of κ [$K = (\kappa^2 - 1)/(\kappa^2 + 1)$]. The angle ψ is defined up to $(\psi + \pi/2) \bmod \pi$.

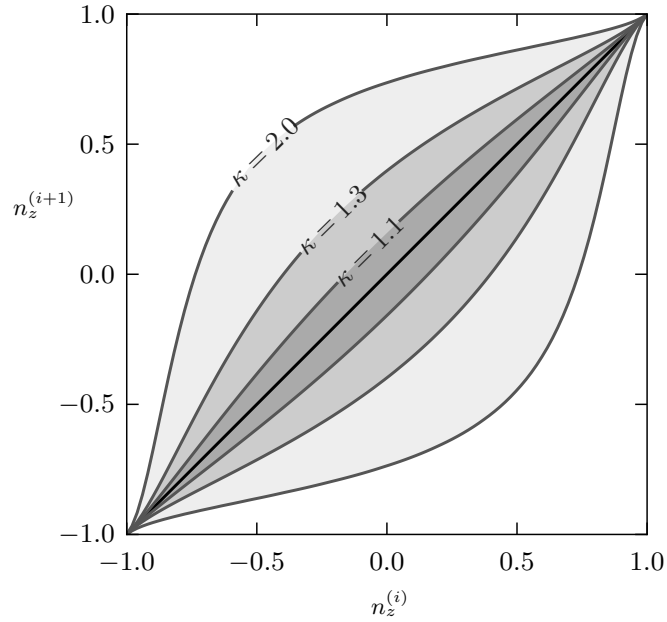


FIG. 7. Range of Poincaré map for $\Lambda = 12/13$ and different values of κ corresponding to the values used in Fig. 6, $K = (\kappa^2 - 1)/(\kappa^2 + 1)$. The data shown was obtained by iterating the Poincaré map once for randomly chosen initial conditions. The initial conditions were determined by sampling ψ uniformly over the surface-of-section for given values of n_z .

numerically integrate the orientational equations of motion for the precise shape of the particle, and to experimentally record the angle ψ . Since the current experimental setup does not allow to reliably extract how the angle ψ changes, we plan to perform experiments with small triangular platelets that will allow to record the angle ψ .

The winding number of the trajectory shown in Fig. 5(d) is roughly 7 corresponding to seven $n_x = 0$ -crossings while the trajectory winds approximately once round the elliptic fixed point in the centre of the surface-of-section. The winding number of the trajectory in Fig. 6(e) is roughly 4 corresponding to four $n_x = 0$ -crossings while the surface winds once around the elliptic fixed point. These observations are in qualitative agreement with the fact that the winding numbers of tori winding around the elliptic fixed points increase as the distance from that point increases (corresponding to larger maximal values of n_z).

Additional results for seven more particles are shown in the Supplementary Online Material⁴², Figs. S1 to S7. In general the results shown in these Figures support the observations and qualitative conclusions summarised above. But the trajectory shown in Fig. S7 is difficult to reconcile with the surfaces-of-section shown in Fig. 6. Fig. S7(c) shows an orbit near $n_z = 0$ where n_z appears not to change sign. But panels (d) and (f) in Fig. S7 show distinct sign changes, not consistent with the surfaces-of-section shown in Fig. 6.

It was pointed out in Section IV that the periods X_p observed in the orientational trajectories can differ substantially between different trajectories of the same particle. Consider for instance particle 1 (Fig. 3). For an axisymmetric ellipsoidal particle ($K = 0$) the Jeffery period (time units) is given by⁵

$$T_p = \pi \frac{\lambda^2 + 1}{s\lambda}. \quad (7)$$

For $K = 0$ this is twice the return time to the surface-of-section. For $K \neq 0$ the return time depends upon the starting position on the surface-of-section, but for small values of K the deviations from (7) are small, of the order of K . For the nearly axisymmetric particle 1 we can use Eq. (7) to estimate the period X_p in Fig. 3. Using the parameters from Table I and assuming that the particle was located at a depth of 60 μm , Eq. (7) gives $X_p \approx 2.3 \text{ mm}$. This is consistent with the range of periods observed in Fig. 3(b) to (f), namely 2.1 mm to 2.6 mm. We infer that the precision in determining the depth at which particle 1 moves through the channel is of the order of one particle length. The variations in periods observed in Figs. 4 and 5 indicate that the actual depths vary more between different panels than in Fig. 3.

VI. CONCLUSIONS

Theory and numerical simulations predict that the orientational dynamics of small neutrally buoyant particles in a shear flow is very sensitive to breaking of axisymmetry^{1,2,15}. Axisymmetric particles tumble periodically on Jeffery orbits, but when the symmetry is broken, the Jeffery orbits are modified. Depending on the initial orientation, periodic, doubly-periodic, or chaotic tumbling may result.

In order to experimentally verify these predictions it is necessary to use particles of well-defined shape, to ensure that inertial effects and rotational diffusion are negligible, and to compare different orientational trajectories (corresponding to different initial orientations) of the same particle.

In this paper we describe measurements of the orientational motion of small glass rods suspended in a micro-channel shear flow. The measurements are precise enough to allow for a definite comparison with theory^{1,2}. First, the glass rods have highly symmetric circular cross sections. Slight imperfections at the ends break the axisymmetry weakly for some particles [Fig. 2(a)]. We also use strongly triaxial particles designed for our purpose by joining two glass rods. Second, by reverting the pressure-driven flow we observe that the orientation retraces its trajectory for many periods. This means that neither inertial effects nor rotational diffusion matter on this time scale. Third by means of an optical trap we change the orientation of the particle, making it possible to measure different orientational trajectories for the same particle.

Our results confirm the theoretical predictions^{1,2}. We observe periodic and doubly-periodic tumbling, and how the nature of the orientational dynamics depends upon the initial orientation, and on the degree to which axisymmetry is broken. Our measurements are consistent with the features of the surfaces-of-section shown in Figs. 6 and 7.

In the future we plan to experimentally map out Poincaré surfaces-of-section (Fig. 6). With the present particles this is not possible because we cannot resolve how the particle spins around its major axis. We therefore plan to perform corresponding experiments using micron-sized triangular platelets. We expect that it will be possible to resolve the tumbling and spinning dynamics of these particles using the methods described in this paper.

ACKNOWLEDGMENTS

We thank S. Gustafsson (Chalmers) for taking the electron-microscope image Fig. 2(a) and for granting us permission to use the image in this paper. B. Mehlig gratefully acknowledges discussions with S. Östlund (University of Gothenburg) on the implications of time-reversal symmetry for the surface-of-section dynamics shown in Fig. 6. This work was supported by grants from the Carl Trygger Foundation for Scientific Research and the Swedish Research Council. Support from the MPNS COST Action MP1305 ‘Flowing matter’ is gratefully acknowledged.

- ¹E. J. Hinch and L. G. Leal, “Rotation of small non-axisymmetric particles in a simple shear flow,” *J. Fluid Mech.* **92**, 591–608 (1979).
- ²A. L. Yarin, O. Gottlieb, and I. V. Roisman, “Chaotic rotation of triaxial ellipsoids in simple shear flow,” *J. Fluid Mech.* **340**, 83–100 (1997).
- ³J. R. Happel and H. Brenner, *Low Reynolds Number Hydrodynamics: With Special Applications to Particulate Media* (Springer, 1965).
- ⁴S. Kim and S. J. Karrila, *Microhydrodynamics: principles and selected applications*, Butterworth-Heinemann series in Chemical Engineering (Butterworth-Heinemann, Boston, 1991).
- ⁵G. B. Jeffery, “The Motion of Ellipsoidal Particles Immersed in a Viscous Fluid,” *Proc. R. Soc. A* **102**, 161–179 (1922).
- ⁶F. P. Bretherton, “The motion of rigid particles in a shear flow at low Reynolds number,” *J. Fluid Mech.* **14**, 284–304 (1962).
- ⁷G. I. Taylor, “The motion of ellipsoidal particles in a viscous fluid,” *Proc. R. Soc. Lond. A* **103**, 58–61 (1923).
- ⁸A. Karnis, H. L. Goldsmith, and S. G. Mason, “The flow of suspensions through tubes. V. Inertial effects,” *J. Chem. Eng.* **44**, 181–193 (1966).
- ⁹G. Subramanian and D. L. Koch, “Inertial effects on fibre motion in simple shear flow,” *J. Fluid Mech.* **535**, 383–414 (2005).
- ¹⁰J. Einarsson, F. Candelier, F. Lundell, J. Angilella, and B. Mehlig, “Rotation of a spheroid in a simple shear at small Reynolds number,” *Phys. Fluids* **27**, 063301 (2015).
- ¹¹J. Einarsson, F. Candelier, F. Lundell, J. Angilella, and B. Mehlig, “Effect of weak fluid inertia upon Jeffery orbits,” *Phys. Rev. E* **91**, 041002(R) (2015).
- ¹²F. Candelier, J. Einarsson, F. Lundell, B. Mehlig, and J. Angilella, “The role of inertia for the rotation of a nearly spherical particle in a general linear flow,” *Phys. Rev. E* **91**, 053023 (2015).
- ¹³H. Brenner, “Rheology of a dilute suspension of axisymmetric Brownian particles,” *International Journal of Multiphase Flow* **1**, 195–341 (1974).
- ¹⁴E. J. Hinch and L. G. Leal, “The effect of Brownian motion on the rheological properties of a suspension of non-spherical particles,” *Journal of Fluid Mechanics* **52**, 683–712 (1972).
- ¹⁵P. J. Gierszewski and C. E. Chaffey, “Rotation of an isolated triaxial ellipsoid suspended in slow viscous flow,” *Can. J. Phys.* **56**, 6–11 (1978).
- ¹⁶C. J. Petrie, “The rheology of fibre suspensions,” *Journal of Non-Newtonian Fluid Mechanics* **87**, 369 – 402 (1999).
- ¹⁷S. Parsa, E. Calzavarini, F. Toschi, and G. A. Voth, “Rotation rate of rods in turbulent fluid flow,” *Phys. Rev. Lett.* **109**, 134501 (2012).
- ¹⁸A. Pumir and M. Wilkinson, “Orientation statistics of small particles in turbulence,” *NJP* **13**, 093030 (2011).
- ¹⁹K. Gustavsson, J. Einarsson, and B. Mehlig, “Tumbling of small axisymmetric particles in random and turbulent flows,” *Phys. Rev. Lett.* **112**, 014501 (2014).
- ²⁰R. Ni, N. T. Ouellette, and G. A. Voth, “Alignment of vorticity and rods with Lagrangian fluid stretching in turbulence,” *J. Fluid Mech.* **743**, R3 (2014).
- ²¹L. Chevillard and C. Meneveau, “Orientation dynamics of small, triaxial-ellipsoidal particles in isotropic turbulence,” *J. Fluid Mech.* **737**, 571 (2013).
- ²²M. Byron, J. Einarsson, K. Gustavsson, G. Voth, B. Mehlig, and E. Variano, “Shape-dependence of particle rotation in isotropic turbulence,” *Phys. Fluids* **27**, 035101 (2015).
- ²³M. Wilkinson, V. Bezuglyy, and B. Mehlig, “Fingerprints of random flows,” *Phys. Fluids* **21**, 043304 (2009).
- ²⁴V. Bezuglyy, B. Mehlig, and M. Wilkinson, “Poincaré indices of rheoscopic visualisations,” *Europhys. Lett.* **89**, 34003 (2010).
- ²⁵M. Wilkinson, V. Bezuglyy, and B. Mehlig, “Emergent order in rheoscopic swirls,” *J. Fluid Mech.* **667**, 158 (2011).
- ²⁶C. Marchioli, M. Fantoni, and A. Soldati, “Orientation, distribution, and deposition of elongated, inertial fibers in turbulent channel flow,” *Phys. Fluids* **22**, 033301 (2010).
- ²⁷J. Einarsson, A. Johansson, S. K. Mahato, Y. N. Mishra, J. Angilella, D. Hanstorp, and B. Mehlig, “Periodic and aperiodic tumbling of microrods advected in a microchannel flow,” *Acta Mechanica* **224**, 2281–2289 (2013).
- ²⁸N. R. Challabotla, L. Zhao, and H. Andersson, “Orientation and rotation of inertial disk particles in wall turbulence,” *J. Fluid Mech.* **766**, R2 (2015).
- ²⁹F. Eirich, H. Margaretha, and M. Bunzl, “Untersuchungen über die Viskosität von Suspensionen und Lösungen,” *Kolloid-Zeitschrift* **75**, 20–37 (1936).
- ³⁰R. C. Binder, “The motion of cylindrical particles in viscous flow,” *Journal of Applied Physics* **10**, 711–713 (1939).
- ³¹J. Trevelyan and S. G. Mason, “Particle motion in a sheared suspensions. I. Rotations,” *J. Colloid Sci.* **6**, 354–367 (1951).
- ³²S. G. Mason and R. S. J. Manley, “Particle motions in sheared suspensions: Orientations and interactions of rigid rods,” *Proceedings of the Royal Society of London. Series A, Mathematical and Physical Sciences* **238**, 117–131 (1956).
- ³³W. Bartok and S. G. Mason, “Particle motion in sheared suspensions,” *J. Colloid Sci.* **12**, 243–262 (1957).
- ³⁴H. L. Goldsmith and S. G. Mason, “Particle motions in sheared suspensions. XIII. The spin and rotation of disks,” *J. Fluid Mech.* **12**, 88 – 96 (1962).
- ³⁵H. L. Goldsmith and S. G. Mason, “The flow of suspensions through tubes. I. Single spheres, rods, and discs,” *J. Colloid Sci.* **17**, 448 – 476 (1962).

- ³⁶E. Anczurowski and S. G. Mason, “Particle motions in sheared suspensions. XXIV. Rotation of rigid spheroids and cylinders,” *Transaction of The Society of Rheology* **12**, 209–215 (1968).
- ³⁷J. B. Harris, M. Nawaz, and J. F. T. Pittman, “Low-Reynolds-number motion of particles with two or three perpendicular planes of symmetry,” *Journal of Fluid Mechanics* **95**, 415–429 (1979).
- ³⁸C. A. Stover and C. Cohen, “The motion of rodlike particles in the pressure-driven flow between two flat plates,” *Rheol Acta* **29**, 192–203 (1990).
- ³⁹T. Kaya and H. Koser, “Characterization of hydrodynamics surface interactions of escherichia coli cell bodies in shear flow,” *Phys. Rev. Lett.* **103**, 138103 (2009).
- ⁴⁰R. Alargova, K. Bhatt, V. Paunov, and O. Velev, “Scalable synthesis of a new class of polymer microrods by a liquid-liquid dispersion technique,” *Advanced Materials* **16**, 1653–1657 (2004).
- ⁴¹E. P. Lewandowski, J. A. Bernate, P. C. Searson, and K. J. Stebe, “Rotation and alignment of anisotropic particles on nonplanar interfaces,” *Langmuir* **24**, 9302–9307 (2008).
- ⁴²Additional experimental data (URL TO BE INSERTED BY AIPP).
- ⁴³J. Einarsson, “Orientational dynamics of small non-spherical particles in fluid flows,” (2013), Licentiate thesis, Department of Physics, University of Gothenburg.
- ⁴⁴S. H. Strogatz, *Nonlinear dynamics and Chaos* (Westview Press, 1994).
- ⁴⁵H. Goldstein, *Classical Mechanics* (Addison-Wesley, Reading, Massachusetts, 1980).
- ⁴⁶A. Politi, G. L. Oppo, and R. Badii, “Coexistence of conservative and dissipative behaviour in reversible dynamical systems,” *Phys. Rev. A* **33**, 4055 (1986).
- ⁴⁷A. J. Lichtenberg and M. A. Lieberman, *Regular and stochastic motion* (Springer, New York, 1983).

Tumbling of asymmetric microrods in a microchannel flow

J. Einarsson,^{1, a)} B. M. Mihiretie,^{1, a)} A. Laas,¹ S. Ankardal,¹ J. R. Angilella,² D. Hanstorp,¹ and B. Mehlig¹

¹⁾*Department of Physics, University of Gothenburg, 41296 Gothenburg, Sweden.*

²⁾*LUSAC, Université de Caen, Cherbourg, France.*

(Dated: 11 November 2021)

^{a)}These authors contributed equally to this work.

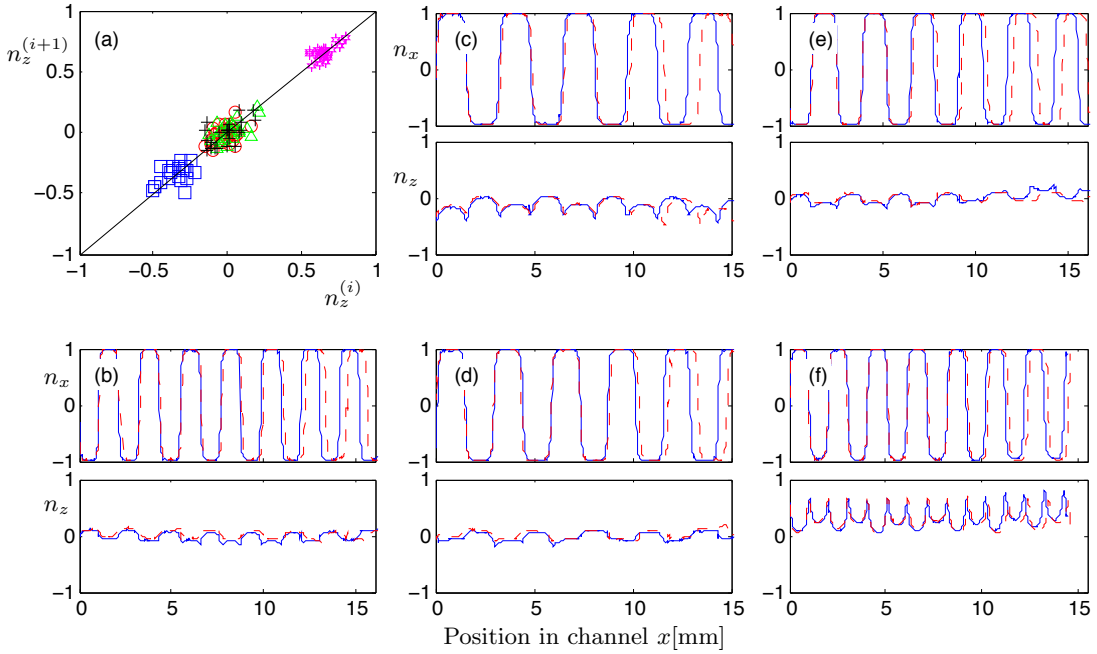
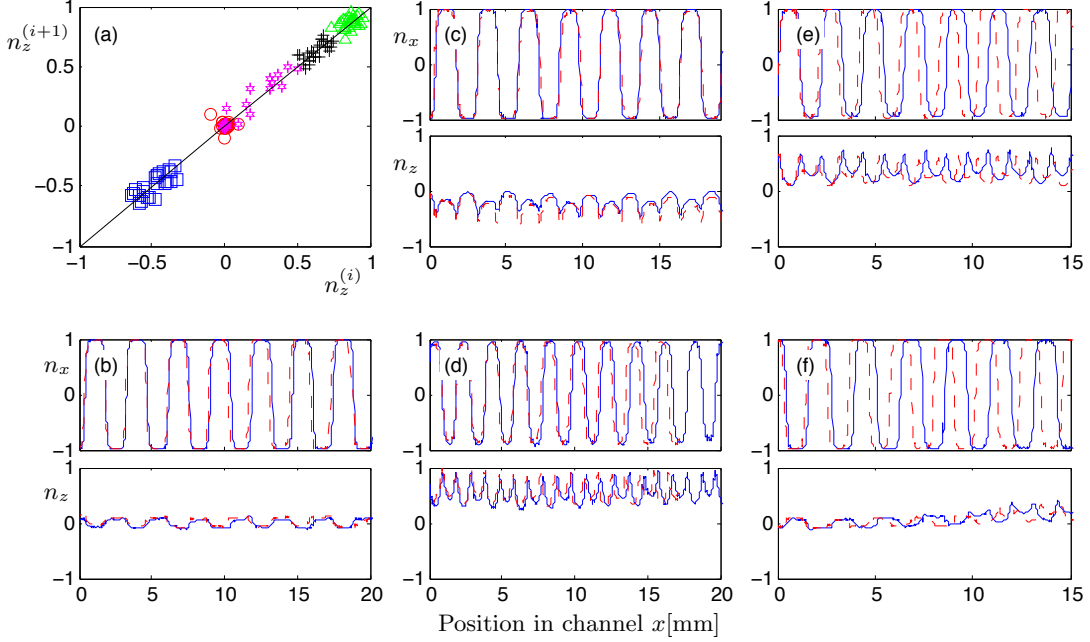


FIG. S2. Orientational dynamics of particle 5.

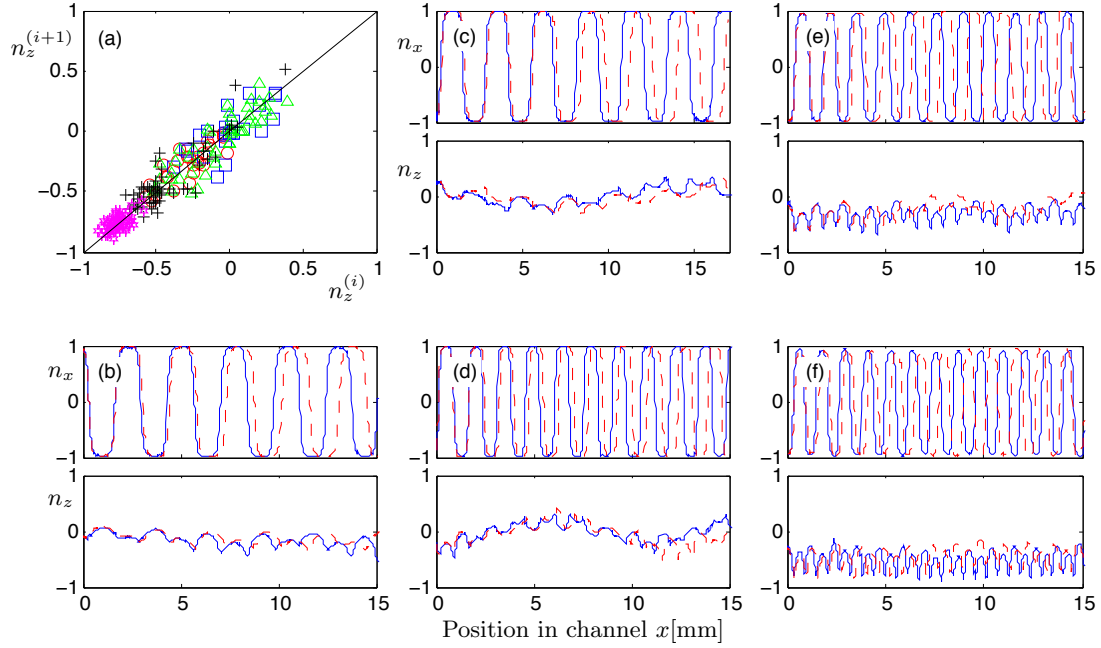


FIG. S3. Orientational dynamics of particle 6.

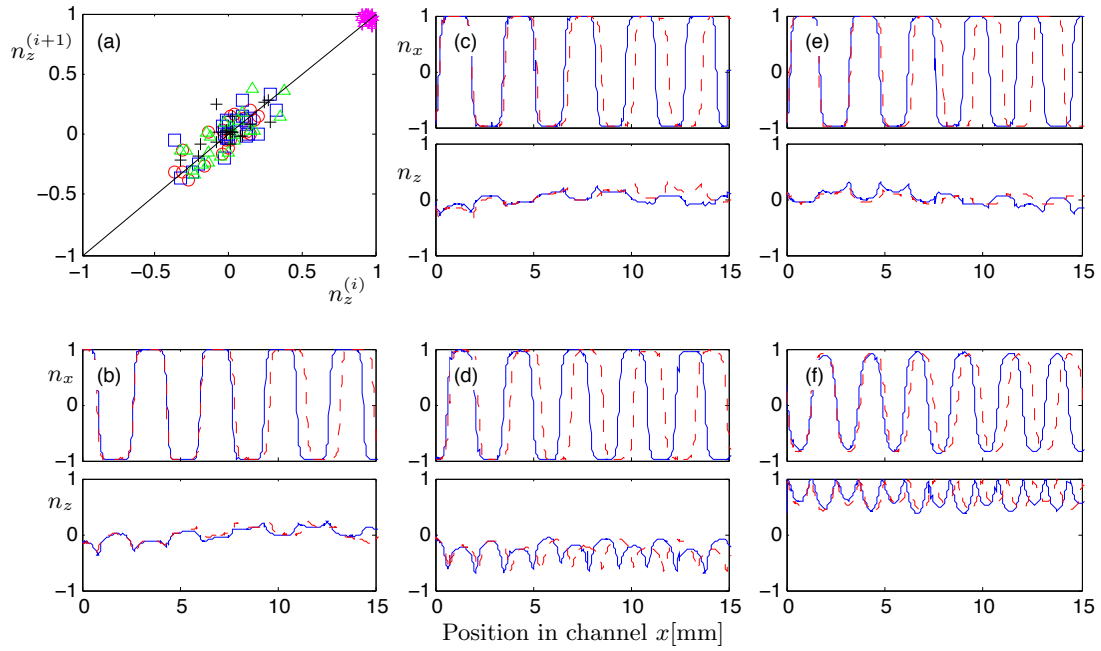


FIG. S4. Orientational dynamics of particle 7.

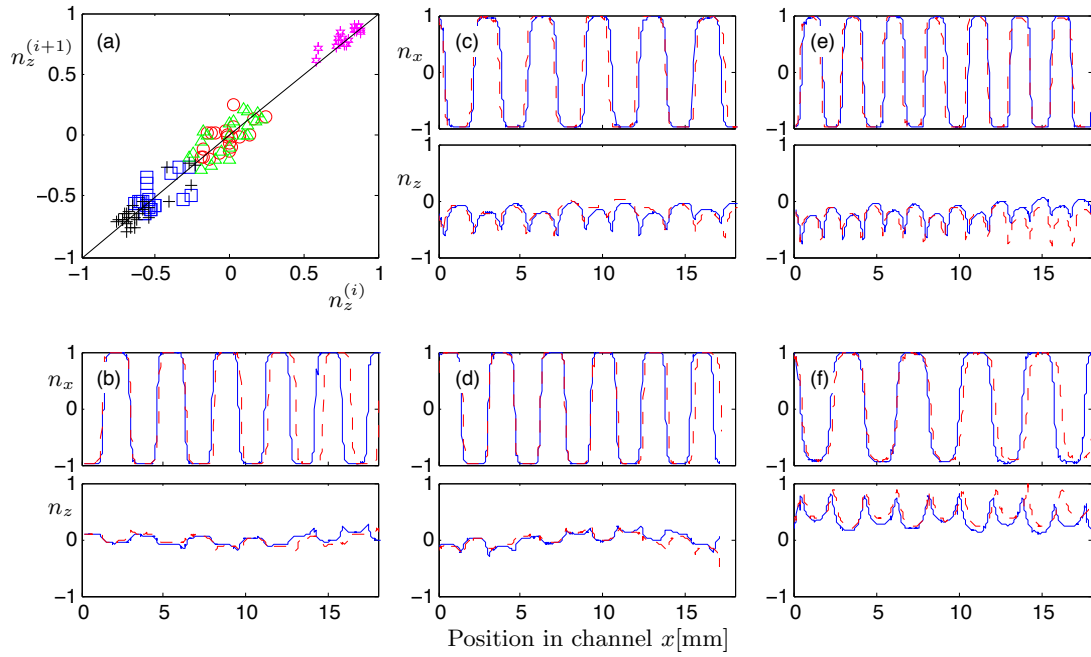


FIG. S5. Orientational dynamics of particle 8.

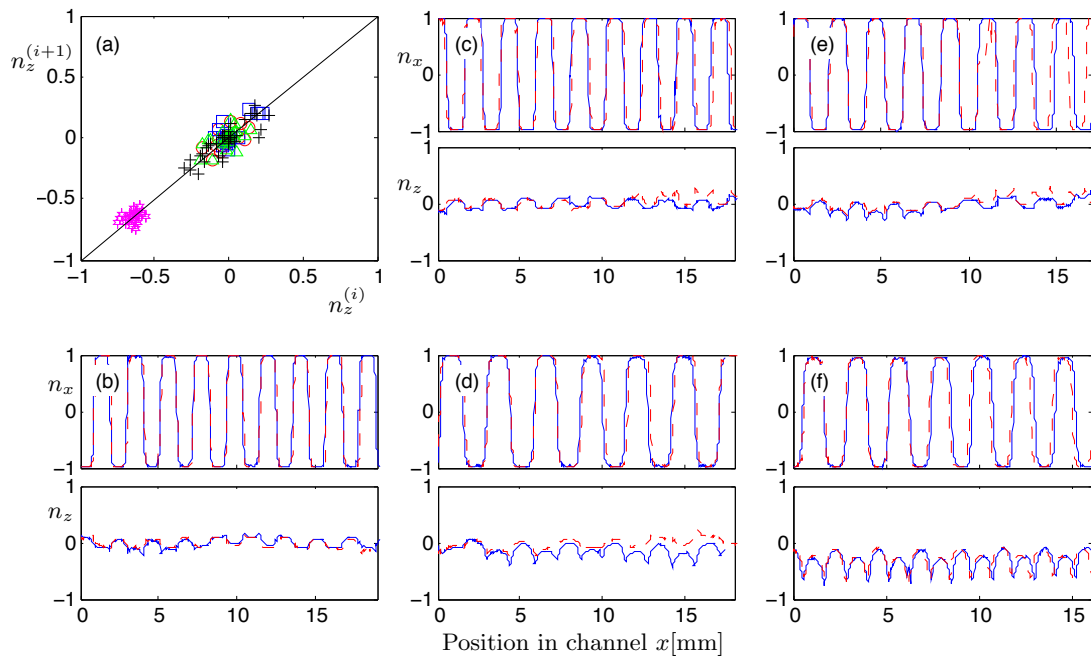


FIG. S6. Orientational dynamics of particle 9.

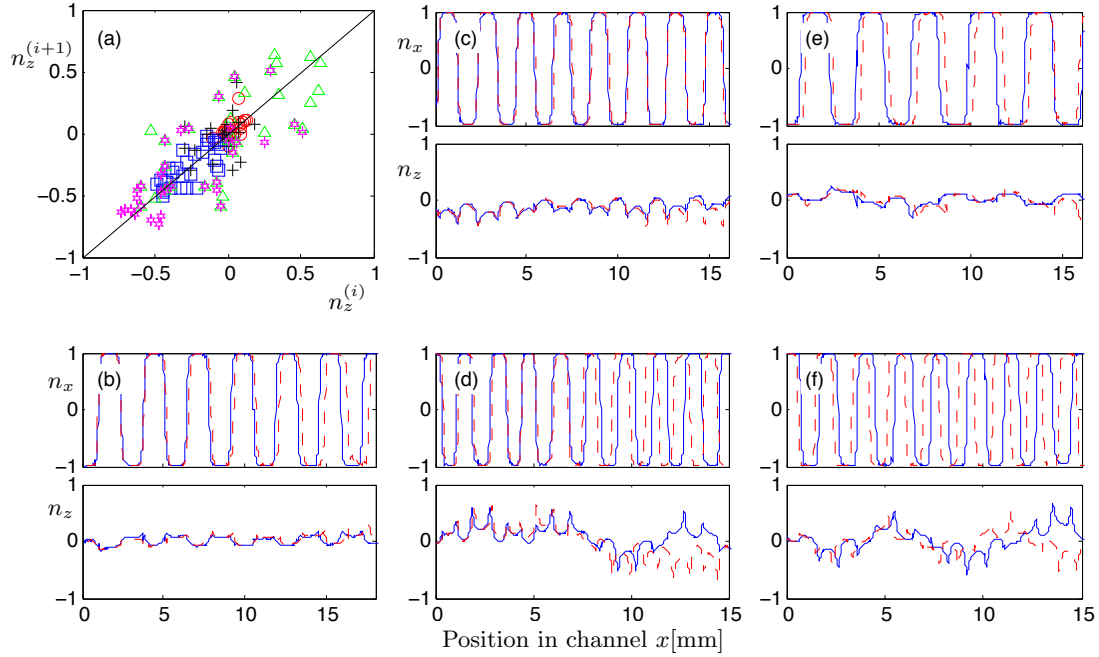


FIG. S7. Orientational dynamics of particle 10.

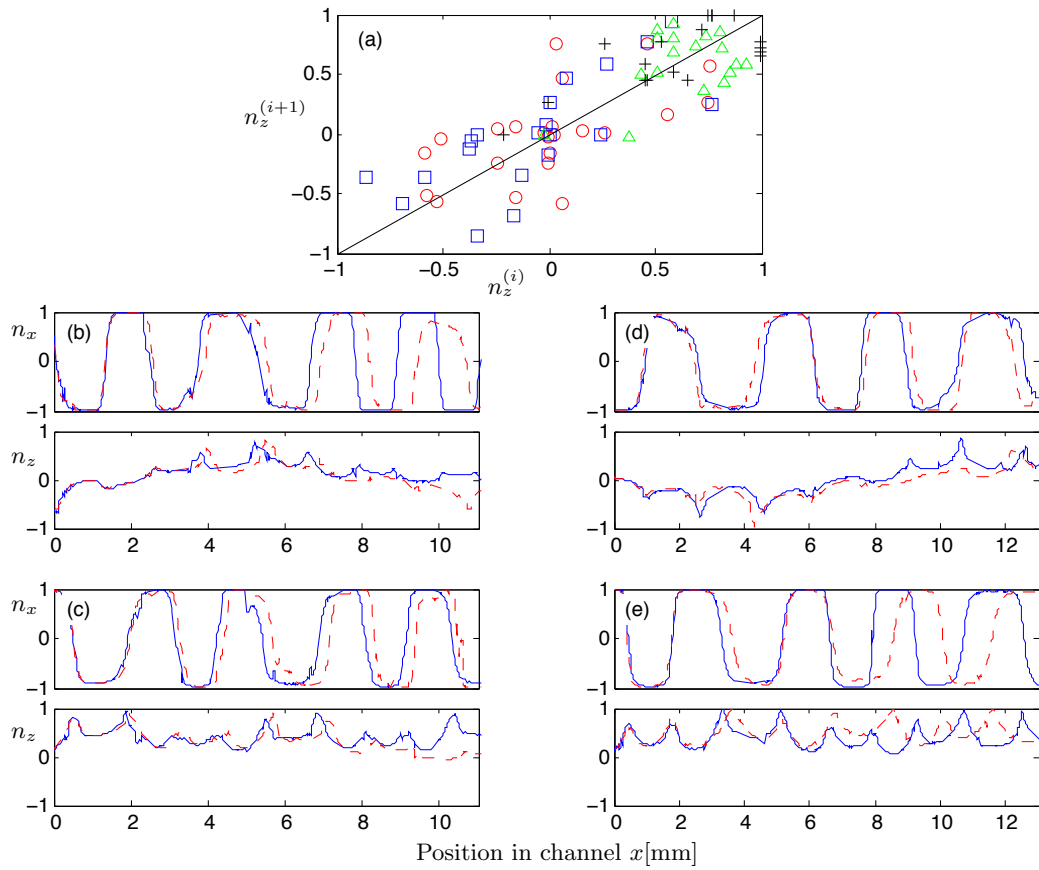


FIG. S8. Orientational dynamics of particle 11.

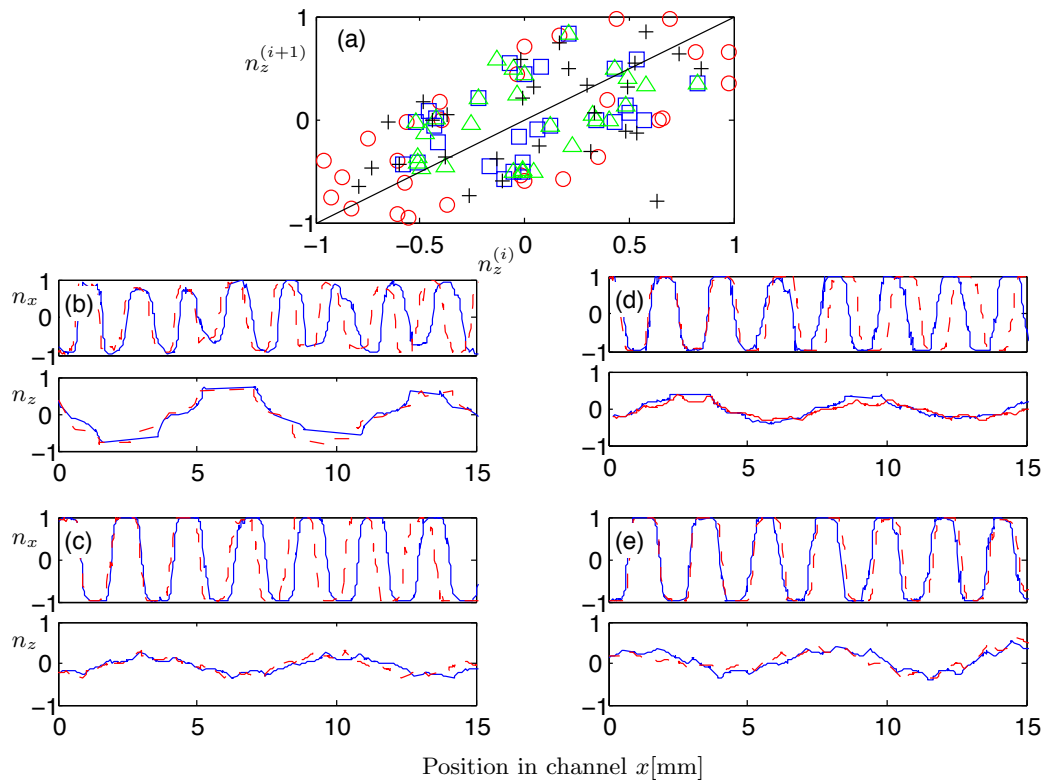


FIG. S9. Orientational dynamics of particle 12.